Curvature-Induced Buckling for Flapping-Wing Vehicles

Mohammad Sharifzadeh and Daniel M. Aukes

***Abstract*—This article explores a technique to leverage curved surfaces for producing preferential buckling that can be used to create forward thrust in flapping-wing devices. We present a novel concept for using anisotropically buckling beams in robot locomotion, facilitated via an analytical and finite-element-based analyses. We demonstrate that with symmetric flapping inputs from a motor, buckling beams can be used to generate forward thrust, power, and work while reducing the drag associated with the recovery phase of the flapping gait. Our analysis includes experimental data that measures the forces produced by wings flapping in air and water. The results show a clear difference in the work produced between buckling and nonbuckling curved beams and shows that the average force and work produced by buckling wings over a number of cycles with symmetric flapping is nonzero. This has been demonstrated on a new, two-fin swimming robot that, through the use of this phenomenon, is capable of reaching an average speed of 0.1 m/s. This article makes it possible for simple motor inputs to produce complex swimming gaits through careful consideration during the mechanical design phase for swimming robots.**

***Index Terms*—Controlled buckling, curved beam buckling, robotics, underwater vehicle propulsion.**

I. Introduction

THIS article explores the role curved surfaces and local buckling can play in the generation of asymmetric locomotion forces for swimming and flapping robots. More specifically, we study how curved slender beams buckle preferentially in one direction under symmetric motor inputs, utilizing this phenomenon to design flapping fins and wings that produce forward thrust and net positive work. We further seek, through a knowledge-based exploration of the design and gait parameters key to understanding this effect, how to exploit the phenomenon of one-sided buckling to create complex flapping patterns that create positive average work across multiple gait cycles in physical prototypes that demonstrate and validate this effect.

Fig. 1 illustrates the overall concept of the proposed wing mechanism. In this design, a wing (or fin) is attached to an electric servo via a compliant, curved beam that buckles at two different points along the positive and negative portion of its force/displacement curve, corresponding to opposite and equal sense bending. Fig. 1(a) shows that controlling the amount of force exerted on the end of the beam in positive and negative directions can avoid buckling in both directions, permit buckling in one direction, or buckle the beam in both directions.

When actuated in a fluid such as air or water, it is our intent to show that the dynamics of powered, symmetric flapping results in one of three general cyclic flapping patterns for the system in question. The first regime is typified of slow flapping below the buckling limit in either direction, where drag and inertial forces remain low [Fig. 1(d)]. In this case, the curved beam acts like a simple bending beam; little asymmetric behavior is observed in its flapping path or in the average thrust generated over a cycle [Fig. 1(e)]. In the second regime—the primary focus of this article—the flapping velocity is sufficient to buckle the beam in the equal-sense bending direction but not in the opposite direction. This results in the beam undergoing large deflections about the buckling point during roughly half of its flapping cycle, which permits the larger surface area of the wing to travel nearly parallel with the direction of motion, rather than perpendicular. This different angle of attack results in reduced drag forces on the wing during the recovery segment of the stroke [Fig. 1(b)]. As the cycle reenters the power stroke, drag causes the wing to open back up in the other direction and remain perpendicular to the direction of motion. This difference in overall drag experienced by the wing in power and recovery phases generates nonzero average work over a single flapping cycle, even with a symmetric input from the motor [Fig. 1(c)]. In the third regime, the beam buckles in both directions due to high torques exerted by the motor that increase the drag and inertial forces experienced at the tip of the beam past the buckling limit in both directions. While also a potentially useful regime, we have observed that, in some cases, buckling in the opposite sense resulted in plastic deformation and rapid failure of the beams. Thus, we have limited our current exploration to the first two regimes in this article.

The rest of the article is organized as follows. Section I-B discusses prior work. In Section II, we describe a flapping wing design in which the buckling characteristics of curved beams can be studied and tuned. We then study the curved

Manuscript received March 7, 2020; revised June 23, 2020 and September 1, 2020; accepted October 20, 2020. Date of publication October 29, 2020; date of current version February 16, 2021. Recommended by Technical Editor T. Seo and Senior Editor X. Tan. This work was supported by the National Science Foundation under Grant 1935324. *(Corresponding author: Daniel Aukes.)*

The authors are with The Polytechnic School, Fulton Schools of Engineering, Arizona State University, Mesa, AZ 85212 USA (e-mail: sharifzadeh@live.com; danaukes@asu.edu).

This article has supplementary downloadable material available at https://ieeexplore.ieee.org, provided by the authors.

Color versions of one or more of the figures in this article are available online at https://ieeexplore.ieee.org.

Digital Object Identifier 10.1109/TMECH.2020.3034659

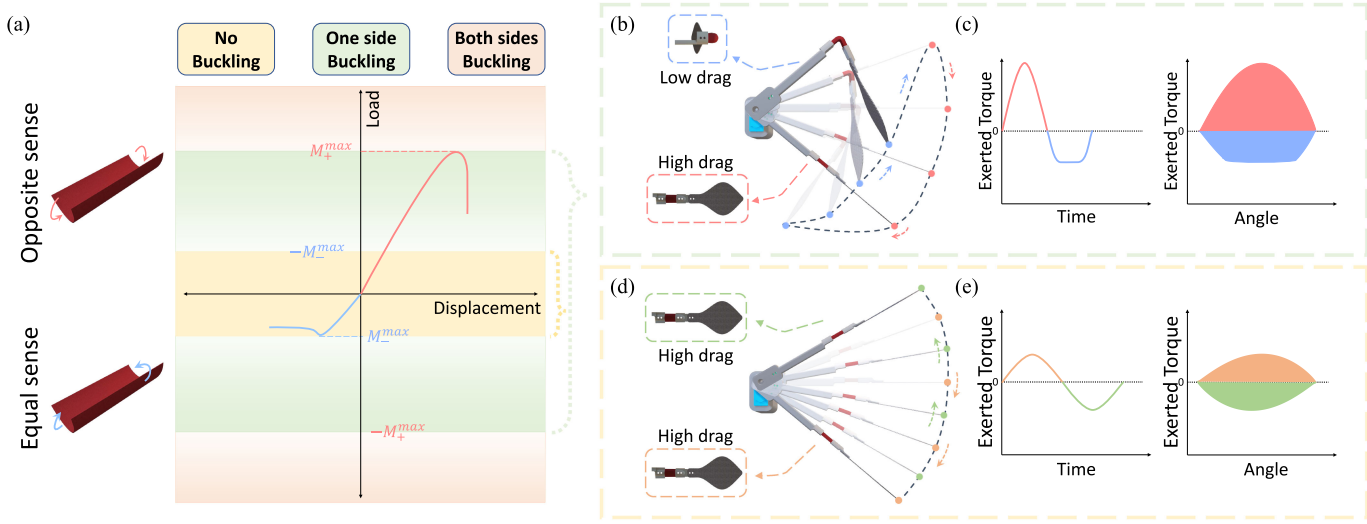

Fig. 1. Conceptual illustration of the proposed technique. (a) Different regimes of a wing with curved beam. (b) Motion of wing in one-side buckling regime. (c) Torque exerted by the wing on a fixed frame with respect to time and joint angle for one-side buckling regime. (d) Motion of wing in no-buckling regime. (e) Torque exerted by the wing on a fixed frame with respect to time and joint angle for no-buckling regime.

beam by discussing the theoretical underpinnings of our idea in Section II-A; we subsequently introduce a finite element analysis (FEA)-based model, which permits us to study curved beam design parameters (Section II-B). Section III introduces a dynamic model of our proposed system that validates this phenomenon in water; Section IV describes experimental validation of the concept in air (Section IV-A) and in water (Section IV-B) on two separate robotic platforms, and finally, Section V concludses this article.

A. Summary of Contributions

Our contributions may be summarized as follows. First, we, for the first time, apply the concept of buckling tape springs for locomotion via flapping in fluids. Second, we select an appropriate analytical framework to understand the effect of buckling in curved beams for use in generating thrust; third, utilize finite-element methods to further study the relationships between design parameters like curvature, length, and width on beam stiffness and buckling limits. Fourth, these relationships are then validated in simulation and experimentally, demonstrating positive nonzero average forces, power, and work (in contrast to regime I introduced above). Finally, we introduce a novel robotic platform that leverages this phenomenon to swim in water.

B. Background

Many structures in nature utilize flexibility and curvature to enhance locomotion capabilities. In some cases, observations of active curvature or cupping in fish [1], [2], 3-D curvature in batoids [3], and flexible flapping of insect wings [4] has been identified as a strategy proposed for optimizing locomotion efficiency throughout a stroke. Walker [5] suggests that the emergence of rowing versus flapping behavior in biological locomotion is a function of viscosity-dominated forces at low Reynolds numbers.

Buckling is also used in the natural world for animal locomotion and other tasks. Camber, deformation, and the "umbrella effect" has been studied in the desert locust [6]–[8]; like an umbrella buckling in a gust of wind, hindwing camber has been observed to rapidly invert between up-stroke and down-stroke. Young *et al.* [8] find that power economy increases 15% when considering the effect of camber in flapping models. Both [6] and [7] identify the buckling of venous structures as the principal mechanism, which permits this inversion. Buckling has also been identified as the principal mechanism for successful locomotion in bacterial flagella, [9], arthropod joints [10], and Venus flytraps [11]–[13], and is used by ladybird beetles as a mechanism to fold and store wings inside their shell [14].

A basic introduction to buckling is typically found in introductory mechanics of materials texts in engineering. Buckling is typically considered a source of catastrophic failure in structures, and models for buckling [15] are introduced in order to avoid it [16], [17]. However, buckling has several characteristics that make it potentially useful in mechanisms and robotics. First, it does not always imply material yield; rather, small geometric perturbations lead to drastic reductions in load-carrying capacity irrespective of the stress in the material. In general, buckling occurs when a material exhibits a nonlinear and often rapid drop-off in force due to small changes in shape. Once a buckling condition is met, the material deforms quickly, resulting in a new force/displacement curve with a much smaller stiffness coefficient. Sometimes the stiffness coefficient can become negative, leading the device to rapidly reconfigure to a new stable state; this condition is referred to as a "snap-through instability" in the literature [18], [19]. In the design process, buckling is typically associated with failure and avoided. In some cases—as in a tape spring or tape measure—this condition is exploited.

When extended with the curved surface opposing gravity, a tape spring can support its own weight on the order of several feet. When flipped over; however, it collapses rather quickly. In addition, a tape spring is able to be rolled into a small volume without fatigue or failure. Clearly, the material properties, design geometries, and selected camber all play an important role in this device's operation.

A variety of prior work investigates buckling and snap-through instabilities with regard to its use as a mechanical device. Work by Koh *et al.* [20] demonstrate a flea-inspired torque reversal mechanism in which energy stored in a spring is released via a small perturbation in the kinematics of a mechanism . In other work a venus flytrap-inspired mechanism utilizes reversible buckling to facilitate rapid inversion between concave and convex states in a shape memory alloy (SMA)-actuated device [21]. In [22], a self-deployed gliding wing is made using characteristics of a curved origami facet. The use of curved facets permits the wing to deploy at its ballistic apex, resulting in an increased gliding range. Jung *et al.* [23] have also proposed a gripper inspired by a caterpillar's proleg that uses flexural buckling for adaptive gripping on rugged, uneven surfaces. In [24], an origami-inspired structure is used to produce dual-stiffness joints by prestretching and sandwiching a flexible material in a multilayer structure during fabrication to induce buckling in the presence of high forces, forming a mechanical fuse. Jiang *et al.* [25] propose a mechanism to reconfigure the stiffness of tubular structures, using pinching to induce highly directional changes in stiffness.

In contrast to prior work, which utilizes complex, origami-inspired mechanisms or uses anisotropy for single-use deployment applications, this article seeks to leverage the simplicity of curved slender beams as passive, nonlinear elements in the active generation of thrust, power, and work via cyclic flapping. Our approach augments prior work in tape spring theory, using FEA to understand and control design parameters such as beam length, curvature, and width to influence the thrust and work generated via symmetric gait patterns. We are motivated by the simplicity of the structures we employ, and our approaches differ from prior analytical methods in that we demonstrate how the nonlinear stiffness produced by such elements is sufficient to describe the dynamic and hysteretic nature of flapping systems in fluid.

Our approach to generate thrust resembles the rowing motion of pectoral fins used by fish in the "labriform" swimming mode [26], [27], in which the objective is to produce thrust using a cyclic motion consisting of power and recovery strokes. Different mechanisms have been proposed to enhance production of propulsive forces during the power stroke while reducing drag forces during recovery stroke. Behbahani *et al.* [27] propose a flexible hinge alongside a hard stop for thrust generation using pectoral fins in a robotic fish. Using flexural joints or fins in combination with a hard stop is studied in other fish-inspired robots [28], water beetles [29], and bird wings [30] as well. The similar approaches used across these robots use system flexibility in the recovery stroke to reduce drag forces while preventing the same flexibility in the power stroke, increasing the average propulsive force over a gait cycle. Similar thrust generation through rowing has been achieved using rigid, curved

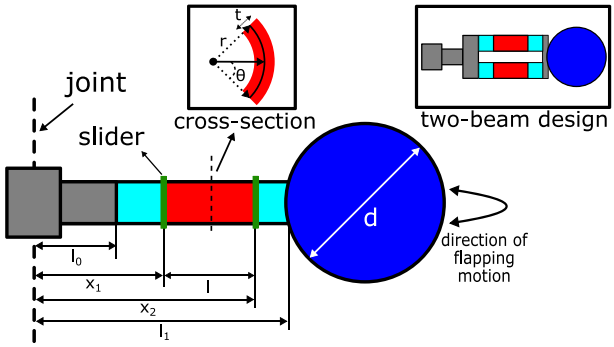

Fig. 2. Side view of our flapping wing designs, with design and experimental variables labeled.

fins [31] as well as active curvature control via multiple actuators [26], [32]. In contrast to the aforementioned solutions, our mechanism produces thrust merely through the asymmetric buckling behavior of curved beams, rather than relying on jointed multibody or multiactuator approaches. This results in a highly nonlinear response that can be tuned and customized based on need, while remaining simple in implementation—control signals at the actuator may remain symmetric using this concept, as the beam's anisotropic stiffness is responsible for breaking swimming symmetry. Tuning can use a wide variety of design parameters—beam length, curvature, thickness, etc—in order to achieve different dynamic performance as a function of the fluid or desired performance criteria (speed, efficiency, power, etc). In this article, we demonstrate how changing effective beam length and flapping frequency can affect the behavior of the system; Future studies will expand on this concept via other parameters in order to optimize for more specific dynamic performance criteria in specific cases and media, as discussed in the conclusions.

II. Analysis of Curved Beam in Anisotropic Buckling Wings

This section details the basic components of anisotropic buckling wings. Subsequently, the section focuses on modeling and characterization of curved beams embedded in these wings. In order to split the problem between aerodynamic and buckling domains, a family of relatively simple wing designs composed of a long thin beam connected to a circular flat plate has been considered. This wing is attached to a joint (defined by the heavy dashed line in Fig. 2) that may be powered by a motor or transmission. The role of the circular plate is to produce thrust and drag and apply resultant forces and torques through the curved beam to the body of a mobile robot. We assume symmetric propulsion throughout the article, though different gait strategies could be selected and studied. This permits us to study the impact buckling and deflection has on thrust and force production as a function of wing configuration throughout its gait cycle.

We model buckling under the assumption of end-loading conditions consisting of point loads and moments from aerodynamic forces in the distal portion of the wing. The wing seen in Fig. 2 comprises several sections: a rigid plastic section

of length l_0 (gray), a section of length $(x_1 - l_0)$ (in cyan), a second interstitial section of length $(l = x_2 - x_1)$ (red), and a third section of length $(l_1 - x_2)$ (cyan), which is connected to a circular plate of diameter d. The curved beam with thickness t is curved along its length via two curved plastic sliding attachments located at x_1 and x_2. These sliders induce a camber to the beam, which can be represented as a radius of curvature r. The cyan and red sections of the wing are made of a single sheet of t-mm-thick polyester, whereas the gray portion is a sufficiently rigid 3-D printed plastic.

For the purposes of our design and analysis, we assume that the position of sliders 1 and 2 is such that the red portion of the beam is the weakest and buckles first in the presence of flapping forces. Though camber of the wing may be observed along the beam, the circular plate does not exhibit significant curvature due to increased material stiffness.

A. Theoretical Model for Curved Beam Buckling

Two different formulations are most often used to describe the buckling phenomenon of curved beams in the literature, namely the buckling of spherical shells [34], [35] and the behavior of folded tape-springs [33], [36]–[39].

In order to understand this phenomenon based on the buckling of spherical shells, Kebadze *et al.* [35] explain that in opposite-sense bending, prestressed, curved material first passes through a flattened state via moments exerted on the shell's edge (M_x and M_y). Stress (σ_y) is the direct result the of curvature change in the y-direction, whereas (σ_x) is caused by Poisson's ratio. Considering that the material remains in its elastic range during this deformation, the stress distribution through the thickness stays linear and stress distribution can be determined.

This model finds critical buckling stress as a function of curvatures of the two stable phases, i.e., initial longitude curvature and final phase curvature. In this article, the system has no second stable phase. As a result, the value for final phase curvature is unknown and the value for critical buckling moment cannot be obtained based on this system of equations.

The behavior of a tape spring is formulated by Wuest in [38], in which moment-curvature relationships for a tape spring subject to equal and opposite end moments are obtained [Fig. 3(a)]. As described by Soykasap [36], end moments can be obtained by integrating of moments about the transverse axis for the whole cross section of the tape spring by considering the beam as a slightly distorted axi-symmetric cylindrical shell. In this formulation

$$M = \int_{-s/2}^{s/2} (M_l - N_l w) dy = sD \times \left(k_l + \frac{\nu}{r} - \nu \left(\frac{1}{r} + \nu k_l \right) F_1 + \frac{1}{k_l} \left(\frac{1}{r} + \nu k_l \right)^2 F_2 \right) \tag{1}$$

where M_l and N_l are the bending moment per unit length and the axial force per unit, respectively. w represents out-of-plan deflection, the y-axis corresponds to the longitudinal direction,

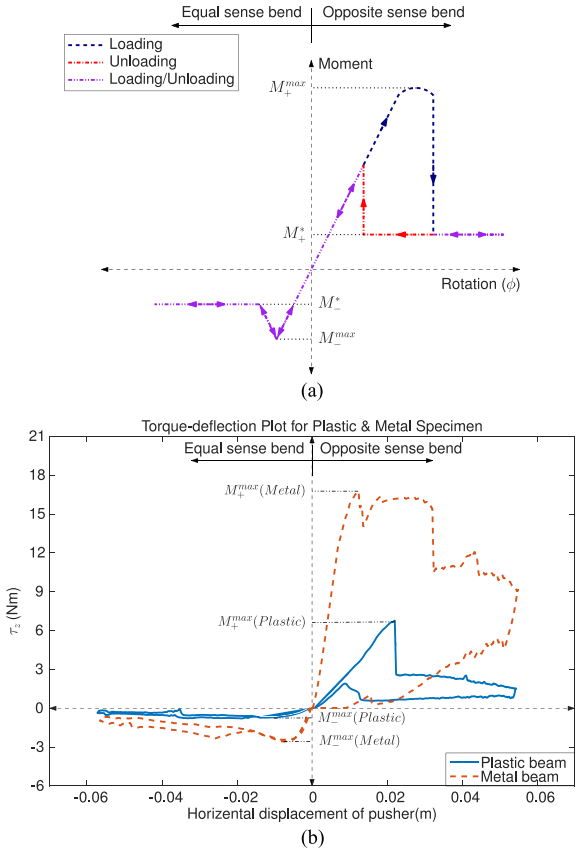

Fig. 3. Nonlinear behavior of a curved beam derived (a) from theory [33] and (b) from experimental data for a steel and plastic specimen with the same geometry. Both results show a considerable decrease in stiffness after buckling occurrence both in opposite and equal-sense bending.

and k_l is longitudinal curvature. s and D are the width of the tape spring and bending stiffness, respectively and can be determined by the following equations:

$$s = 2r \sin\left(\frac{\theta}{2}\right) \tag{2}$$

$$D = \frac{Et^3}{12(1-\nu^2)} \tag{3}$$

where E, ν, and t are Young's modulus, Poisson's ratio, and tape spring thickness, respectively. r and θ are the initial transverse radius and curvature angle of tape spring, respectively. F_1 and F_2 in (1) are calculated as follows:

$$F_1 = \frac{2}{\lambda} \frac{\cosh\lambda - \cos\lambda}{\sinh\lambda + \sin\lambda} \tag{4}$$

$$F_2 = \frac{F_1}{4} - \frac{\sinh\lambda \sin\lambda}{(\sinh\lambda + \sin\lambda)^2} \tag{5}$$

$$\text{where } \lambda = \frac{\sqrt[4]{3(1-\nu^2)s}}{\sqrt{\frac{t}{k_l}}} \tag{6}$$

The critical buckling moment ($M_+^{\max}$), can be calculated by finding the maximum end moment in (1). The "steady moments" M_+^* and M_-^* referenced in [36] can be calculated by considering that the curved region is approximately cylindrical

$$M_+^* = (1+\nu)D\theta \tag{7}$$

$$M_-^* = -(1+\nu)D\theta \tag{8}$$

Although M_-^* and $M_-^{\max}$ are considered different values by [33], they are considered equivalent in other studies, which changes the equal-sense bending curve in Fig. 3(a) to a simpler horizontal line starting from $M_-^* = M_-^{\max}$ [36]. Additionally, we note that this formulation is limited to the linear regime of the material's stress/strain curve.

In order to evaluate the theoretical model and provide better understanding of the curved beam, two specimens of a steel measuring tape and a curved polyester beam are considered. Both specimens have the same length (l). The polyester specimen is precurved so as to have the same radius of curvature (r) as the steel specimen. For each specimen, the curved beam is attached at one end to a fixed plate, while a known force is applied to the other end. A force sensor mounted to the output of a linear actuator pushes on the beam via a small, 3-D printed contact point. The linear actuator moves back and forth through a 50 mm range in 10 μm increments; applied forces are sampled at each step.

Fig. 3(b) depicts the result for both specimens in two cases of equal and opposite-sense bending. Both polyester and steel specimens exhibit the buckling behavior predicted in the theoretical model. This may be seen in the sudden drop in the resultant moment at high deflection. The buckling moments in opposite-sense bending ($M_-^{\max}$) are much higher than the equal-sense buckling moment ($M_+^{\max}$) for both specimens. However, there are some notable differences between the theoretical model and experimental data. In both specimens, the deflection of the specimens in Fig. 3(b) does not follow the same path after buckling when forces are removed. This difference is more noticeable in the steel specimen compared to the polyester specimen. In the steel specimen, the values for M_+^* and $M_+^{\max}$ are different (as predicted in [33]), but in the polyester specimen, they have the same value (as predicted in [36]). The sudden change in the experimental torque/displacement data is believed to be due to out-of plane deformation, pusher slip, and friction. Moreover, in the case of opposite-sense bending, the path during loading and unloading of the polyester specimen is closer to the theoretical model predicted in [33] and [36] than the steel specimen. We attribute this to plastic deformation that was observed in the steel specimen. While the theoretical model assumes that the buckling beam does not leave the elastic region, our experiments show otherwise. This can be due to the fact that, like the drag force on the wing, the pusher produces a combination of force and moment on the edge of the curved beam instead of a pure moment. This force-moment combination produces a nonuniform stress distribution on the shell and, in some cases, deforms the plate after buckling in ways not predicted by [33] and [36]. This deformation results in permanent damage to the beams if the moment exceeds ($M_-^{\max}$). As a result, a safe region must be defined for the moment produced by the wing to ensure that the beam never undergoes opposite-sense buckling.

B. FEA Study on Curved Beam Buckling

In order to customize the buckling behavior of curved beams, various design parameters can be adjusted, including the radius of curvature (r), beam width ($r\theta$), beam length (l), and other material properties. FEA may be used to better understand and tune the relationship between these parameters and the desired buckling conditions. Unlike the analytical formulation, which is based upon uniform geometry and specific loading assumptions, FEA methods permit us to explore a wider range of geometries with more nuanced loading combinations as our use of this technique moves toward design optimization.

We, thus, study behavior of a slender curved beam, varying the curvature (θ), length (l), and width ($r\theta$) of the beam as primary design parameters and monitor the change in buckling factor of safety in linear, eigenvalue-based approach. To simplify the analysis we model half the beam and apply a symmetric constraint for the other half; we use a curvature-based mesh setting with a maximum element size of 0.4 and 0.02 mm tolerance. The proximal edge of the beam is fixed while a load is applied to the distal end. The load is a combination on nominal force and moment (1 N and 1 Nm).

First, we demonstrate how adjusting the camber (or longitudinal curvature) of a beam can be used to alter the beam's stiffness and critical load to produce asymmetric flapping cycles and nonzero thrust. The curvature, θ, is defined in Fig. 2 so that $\theta = 0$ corresponds to a flat plate and $\theta = 180$ produces a half-cylinder. Using the results of an FEA study performed using SolidWorks simulation, seen in Figs. 4(a) and (b), the deflection of a curved beam (of dimensions $l = 25.4$ mm by $r\theta = 25.4$ mm by $t = 1$ mm) loaded in equal and opposite sense differs noticeably.

A further study, shown in Fig. 4(c), shows the evolution of the differences in critical load for equal and opposite-sense bending as the curvature of a beam is varied between 30° and 180°. The width ($r\theta$) and length (l) of the undeformed half-beam is set to 25 mm in this article, and the resulting critical loads are obtained when loads are applied in the equal and opposite orientation using a linear eigenvalue-based analysis. The results in Fig. 4 show the magnitude of the buckling factor of safety in equal-sense (blue) and opposite-sense (red) loading cases. While exceeding the opposite-sense buckling limit leads to plastic deformation and should be avoided (as discussed in the previous section), exceeding the equal-sense buckling force reduces drag in the up-stroke portion of the swimming gait and increases the average thrust produced in swimming gaits without leading to beam failure. The black arrows in Fig. 4 show the magnitude of the difference between critical load in either direction, corresponding to the safe working range for using drag forces to create asymmetric flapping gaits without material failure in the beam.

To further understand the relationship of beam width on buckling point, the curvature (θ) and length (l) of the undeformed beam are fixed at 180° and 25.4 mm, respectively, whereas the

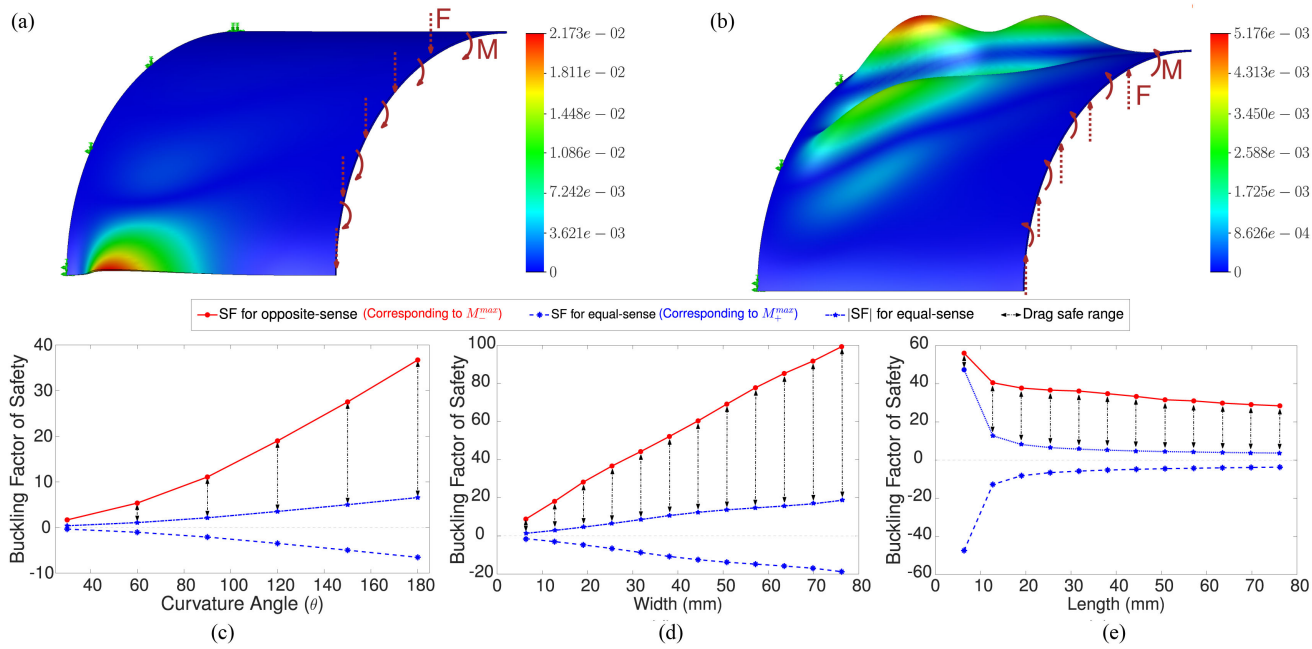

Fig. 4. FEA on the curved slender beam. Side view of the deformation of a thin beam of dimensions 25.4 mm by 25.4 mm and $\theta = 180^\circ$ at its critical load. (a) Equal-sense. (b) Opposite-sense bending. Only half of the symmetric beam is simulated and displayed. FEA results demonstrate the buckling limits as a function of various design parameters in opposite and equal-sense bending, which relate to the differences in load-carrying capability in either direction. (c) Effect of curvature angle (θ). (d) Effect of width ($r\theta$). (e) Effect of length (l).

width of the beam is varied from 6.4 to 76.2 mm. The beam's, radius of curvature (r), volume, and mass change as a function of width. Fig. 4(d) shows the result of this article, where the factor of safety corresponding to both equal and opposite-sense buckling increases as the width of the beam grows. The results also show that the difference in magnitude between equal and opposite-sense buckling limits (black arrows) grows with width.

In order to better understand how beam length (l) impacts buckling, we vary the length of the beam from 6.4 to 76.2 mm while keeping the curvature (θ) and width ($r\theta$) of the undeformed half-beam fixed at 180° and 25.4 mm, respectively. The beam's volume and mass change as a function of length (l) while the radius of curvature (r) is held constant. Loading conditions are varied as a function of l in this since the loading conditions on the buckling portion of the system are defined by the moment and force combination generated by the forces exerted at the distal end of the beam.

The result of this article shows that the buckling limit decreases for both equal and opposite-sense buckling as the length grows [Fig. 4(e)]. However, the difference between the magnitude of positive and negative buckling limits initially grows and then stays somewhat constant for $l > 25.4$ mm.

Based on these results, we have selected a curved beam with $\theta = 180^\circ$ for the rest of the article. The beam length (l), width ($r\theta$), and thickness (t) remain free design variables that can be tuned in order to maximize the effects of one-sided buckling for use in conjunction with the drag and inertial forces acting on the fin across fluids of different viscosity. Future work will require a more systematic search for the optimal design through all parameters to find designs which improve performance for criteria such as speed, efficiency, or power.

III. Dynamic Modeling of Buckling Wing Propulsion

This section describes the dynamic modeling of the system by considering dynamic elements such as wing drag, curved beam stiffness, and rigid body dynamics.

We have modeled the dynamic behavior of a wing system based on these relationships. In this article, a wing system [shown in Fig. 5(a)] is connected to the ground at the base of the input joint and the moments exerted on the environment about the rotational axis are recorded similar to our experimental setup in Section IV-B. The system is represented by two rigid links with point masses located at their centers of mass, connected by a pin joint and torsional spring, with stiffness coefficient of K, connected in parallel. The nonlinear stiffness of the spring is represented by three linear regimes; the slopes of each of these regimes have been adjusted to best fit experimental data collected from our prototype introduced in Section IV-B using the methods discussed in Section II-A.The length (d_1 and d_2) and mass (m_1 and m_2) of each link match the measured values of the in-water prototype from Section IV-B.

Using a flat plate model, the forces on a wing due to a fluid are estimated by the equations derived from [40]:

$$F_{w_D} = \rho u^2 \, A \sin^2 \alpha \tag{9}$$

$$F_{w_L} = \rho u^2 \, A \cos \alpha \sin \alpha \tag{10}$$

where ρ, u, A, and α are the density of fluid, the relative velocity of the plate, the area of the plate, and the angle-of-attack of the wing, respectively. F_{w_D} and F_{w_L} correspond to the drag and lift elements of the aerodynamics forces on the plate. This model

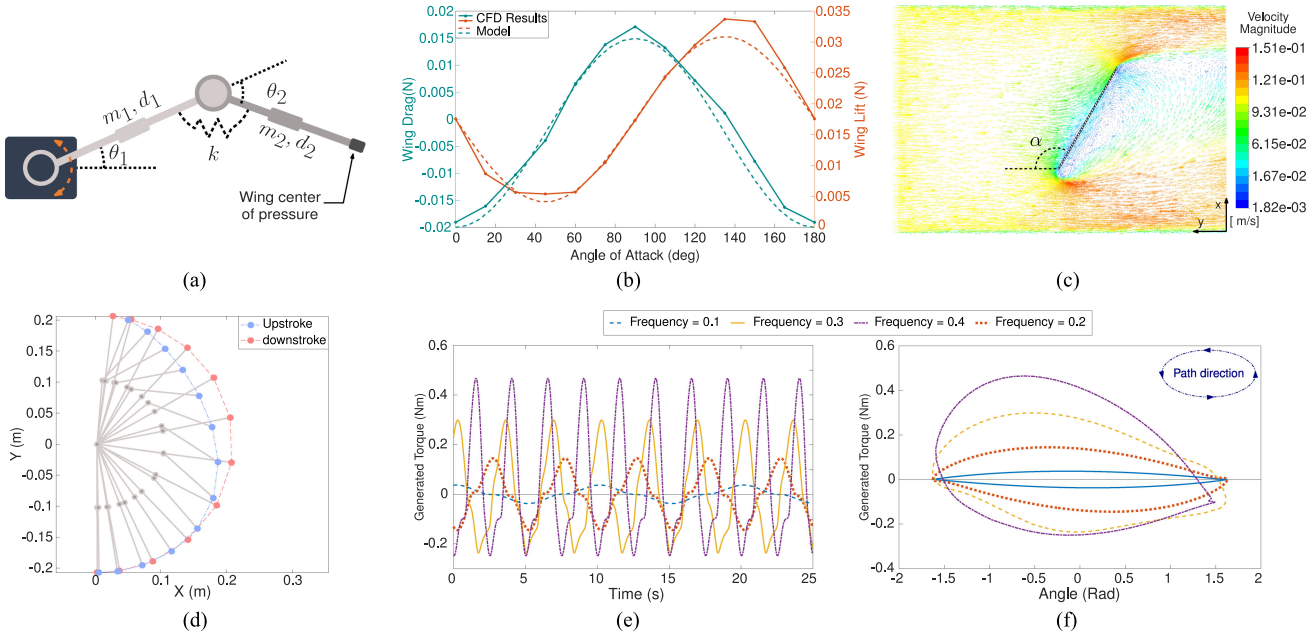

Fig. 5. Dynamic modeling of a wing flapping in water. (a) Model for the wing system. (b) Comparison between the average values of wing lift and drag between flat plate model (9) and (10) and CFD analysis. (c) Velocity magnitude of the water flow in CFD analysis for $\alpha = 120°$. (d) Motion of the wing flapping at 0.4 Hz experiencing buckling during the recovery phase. (e) Torque exerted by the wing on the fixed frame with respect to time. (f) Motor position.

estimates the total force on a flat plate as

$$F_w = \rho u^2 \, A \sin\alpha \tag{11}$$

where α is 0 when parallel to the flow and 90° when perpendicular (in 2-D) [40]. This force is perpendicular to the wing and acts as the aerodynamic load on the curved beam [Fig. 1(a)].

Using (11), we can use the velocity of the plate (u) to control the amount of drag force exerted on it, which, in conjunction with the load limits determined by the mechanics of the curved buckling beam [(1), (7), and (8) and Fig. 3(a)], determines whether and under what conditions buckling occurs.

The flat plate model best describes the fluid dynamics of a system when the Reynolds number is low and the system is in the laminar regime. The Reynolds number of a flapping wing in fluid is formulated as follows [41], [42]:

$$Re = \frac{\bar{u}\bar{c}}{\nu} \tag{12}$$

where $\bar{u}$, $\bar{c}$, and ν are the mean translational velocity of the wing tip, the wing mean chord, and the kinematic viscosity of the fluid, respectively. For the given flapping system, $\bar{u} = 2\Phi f R$, where Φ and f are flapping peak-to-peak angular amplitude and frequency and R is moment arm to the center of pressure of the wing. For this wing flapping in water, the Reynolds number varies from 1800 to 7200 when the flapping frequencies varies from 0.1 to 0.4 Hz, indicating that the flow regime changes from laminar to turbulent at higher flapping frequencies.

We then compare the flat plate model using a computational fluid dynamic (CFD) analysis on the system wing. In this article, carried out in ANSYS [Fig. 5(c)], we have measured the average lift and drag exerted on the wing by uniform water flow with different flowrates as the angle-of-attack varies from 0 to 180°. Fig. 5(b) shows the CFD analysis results for the flow of 0.1 m/s versus the flat plate model estimation. These plots show the high correlation between the flat plate model and CFD results for the latter speed for which the system is in laminar regime. At the maximum studied flapping frequency, the mean transnational velocity of the wing reaches 0.41 m/s for which, in the worst case, the maximum error between flat plate model and CFD results is less than 15%.

When a sinusoidal torque input is applied to the base joint, the dynamic model demonstrates that the wing system transitions between a nonbuckling flapping regime to a one-sided buckling regime [as shown in Fig. 1(a)] when the flapping frequency is increased. Fig. 5(e) and (f) plots the torque produced across different input frequencies as a function of time and base joint angle. From these data we can see that the wing system transitions from the nonbuckling regime to one-sided buckling at around 0.3 Hz. While the maximum positive torque increases with frequency in the power stroke, the torque in the recovery section remains low. The amount of work performed on the environment, in Fig. 5(f), also grows with the emergence of buckling. Fig. 5(d) shows the motion of the modeled wing through a full flapping cycle at 0.4 Hz, behavior which is similar to the in-water flapping behavior shown in Fig. 8(b) and (c).

IV. Experimental Validation

The goal of this section is to experimentally verify the effect of curvature on buckling force for a curved beam, as well as to demonstrate its potential for creating thrust and motion. We have considered two case studies (air and water) to validate our

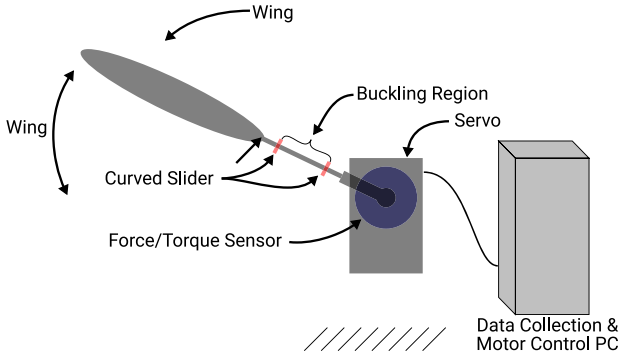

Fig. 6. Experimental setup for measuring air drag applied to wing.

proposed methodology in order to underscore the generality of this concept, using the design principles from the previous section as a design guide.

A. Case Study I: Wing Flapping in Air

In this case study, the air drag exerted on a wing utilizing curved beam buckling is experimentally measured. Our experimental setup is shown in Fig. 6. A dc servo is attached to a flapping wing via a 3-D printed mount, permitting rapid swapping of different wing designs. Forces and torques generated by flapping are measured with a six-axis ATI Mini40 force/torque sensor mounted to the motor and ground. The servo's position input signal is a triangular wave with a fixed amplitude of 66°; the frequency is varied in order to change the aerodynamic interactions experienced by the wing.

1) Variable Length (One Beam): Two different cases of symmetric flapping are studied to demonstrate the effect of anisotropic buckling. In the first case, the sliders are brought closer together; this shortens the exposed beam length (l) and prevents buckling in both directions of flapping and results in similar angle of attack and drag in both up-stroke and down-stroke [orange line in Fig. 7(a), (b), and (c)]. In the second case, curved, reinforcing sliders are arranged so that the gap between them is large enough to permit buckling in the equal-sense direction to occur during sinusoidal flapping. This longer buckling region allows the curved beam to buckle under drag forces in equal-sense bending, but is not sufficient to induce buckling in the opposite sense [blue line in Fig. 7(a)–(c)]. The start and end points of buckling are illustrated in Fig. 7(a) and (b) using red circles and blue squares, respectively. Non buckling and one-sided buckling regions for a full cycle are also shown using light gray and gray boxes.

Fig. 7(b) and (c) shows the moment generated by the wing during symmetric flapping as a function of the wing's angle and speed, respectively. The shape of the nonbuckling curved beam's work loop is qualitatively symmetric (about torque $\tau = 0$), indicating that the average work—the area of the work loop in the positive τ domain minus the area of the work loop in the negative τ domain—over several flapping cycles provided by a nonbuckling beam (orange) is near zero. In contrast, the buckling beam (in blue) shows an asymmetric path (about torque $\tau = 0$), capable of producing nonzero work in the forward direction. This asymmetry is also noticeable in vertical portion of the blue line in Fig. 7(c), shown by vertical double arrows lines, where the positive angular velocity is much smaller compared to the negative side. The abovementioned changes in power and work plots show the effectiveness of anisotropic buckling during symmetric flapping in generating nonzero thrust, power, and work.

TABLE I
TORQUE AND WORK GENERATED DURING FLAPPING IN AIR

Experiment	Frequency (Hz)	Average Torque (Nm)	Work (J)	Mechanical Efficiency	Buckling
Variable Length	2.28	-0.012	-0.009	1.86%	No
	2.28	0.131	0.165	29.50%	One side
1 Beam	1.38	-0.005	-0.005	2.98%	No
	2.06	0.149	0.154	26.73%	One side
	2.28	0.131	0.165	29.50%	One side
2 Beams	2.06	0.004	0.013	2.29%	No
	2.28	0.031	0.019	2.56%	One side
	2.48	0.077	0.095	10.30%	One side

The results demonstrate that the curved beam produces work in symmetric flapping when it is permitted to buckle. The average torque generated over one flapping cycle increases from 0.009 to 0.165 Nm in the presence of unidirectional buckling (Table I). Though the wing-beam system is not optimized for energy efficiency, the mechanical energy efficiency increases from 1.86% to 29.5%. This is calculated by evaluating the ratio of useful work done over the total work done across a full flapping cycle.

2) Variable Frequency (One Beam): We next look at the effect of drag on buckling by increasing the frequency of the triangular input signal for the same curved beam. Plots in Fig. 7 show the torque generated via a symmetric flapping gait with respect to time (a,d,g), servo angle (b,e,h), and angular velocity (c,f,i). In Fig 7(d)–(i), the results for the three flapping rates of 1.38, 2.06, and 2.28 Hz are depicted in blue, red, and orange colors, respectively. In these figures we see that the torque generated by each successive increase in flapping speed increases the magnitude of torques experienced in the positive y domain without similar magnitude increases in the negative y domain. This results in work performed on the environment, which can be seen as a clockwise work loop in both the torque versus servo angle and torque versus angular velocity plots in Fig. 7(e) and (f). At 1.38 Hz, the beam experiences no buckling; however, the faster two cases (2.06 and 2.28 Hz) result in one-sided buckling. The average torque, amount of work done on the environment, and mechanical efficiency are reported in Table I. The data reveal that the buckling duration of a full flapping cycle increases from 25% to 42% in one-sided buckling cases between 2.06 and 2.28 Hz. We note that though the hysteretic gaits obtained here via anisotropic buckling during flapping resembles gaits generated by other techniques such as the split cycle method in [43], the effect in our case is a result of designed system dynamics rather than asymmetric motor inputs.

3) Variable Frequency (Two Beams): To address the nonnegligible torsional effects visible in the wing during flapping, we stiffened our system in torsion by attaching two beams—40 mm

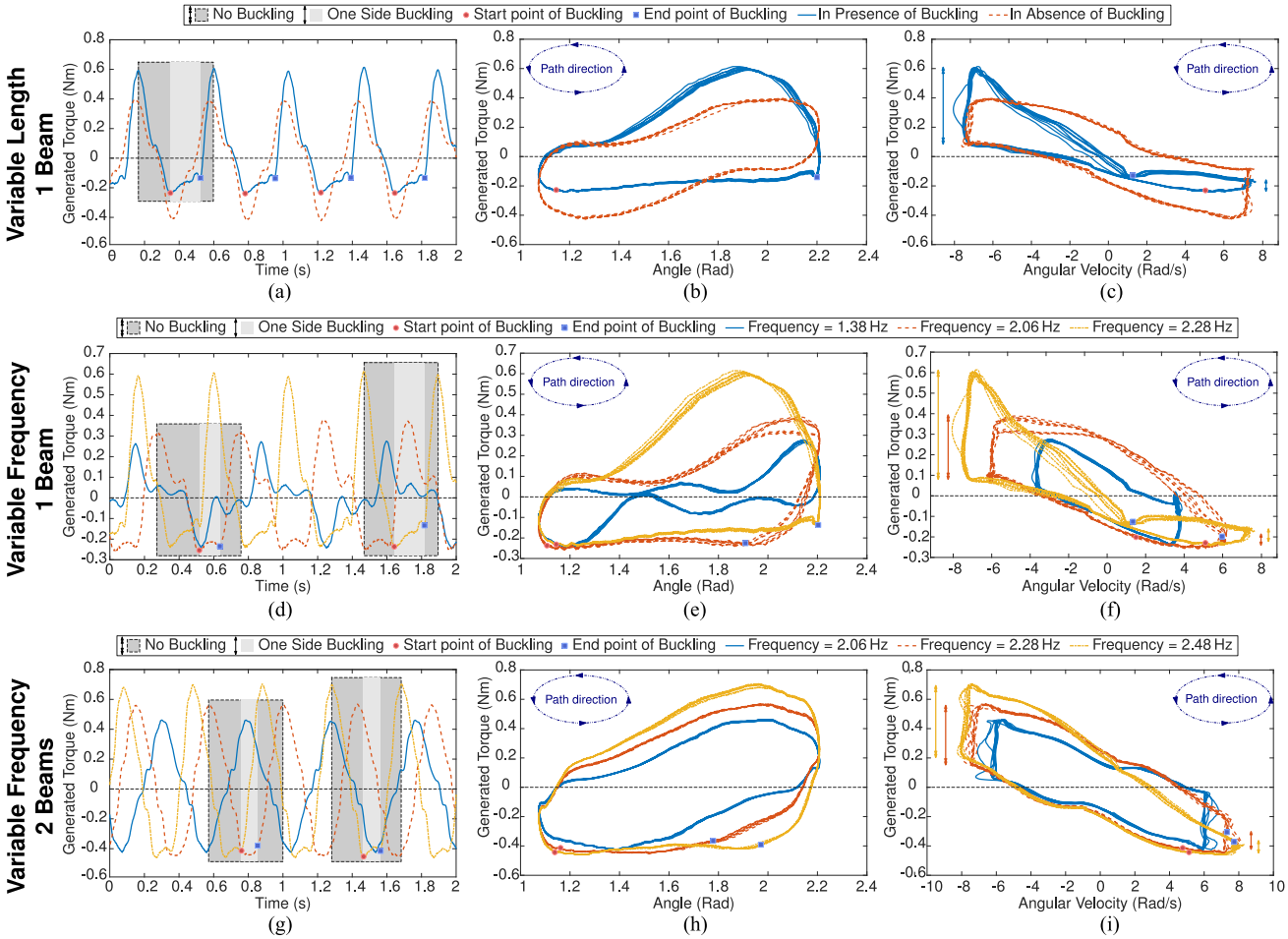

Fig. 7. Effect of asymmetric buckling on a wing flapping in air : (left plots) Torque versus time, measured over several flapping cycles, (middle plots) position versus torque; (right plots) velocity versus torque (a,b,c) One beam with variable effective buckling length that produces no buckling and buckling, respectively. (d,e,f) One beam connected to the wing flapping at 1.38, 2.06, and 2.28 Hz. (g,h,i) Two beams connected to the wing, flapping at 2.06, 2.28, and 2.48 Hz.

apart from each other, in parallel—to the wing, as depicted in Fig. 2. This reduced the noticeable effects of torsion on long thin beams (as noted by [44]) and produced slightly different torques throughout flapping cycles at different speeds. Fig. 7(g)–(i) shows the results of this test at 2.06 (blue), 2.28 (red), and 2.48 (orange) Hz, respectively. The results show similar trends and behavior with the previous one-beam case, but because the system is stiffer (due to two beams in parallel), it takes higher velocities (and higher drag) to initiate buckling. This can be seen in the of 2.06 Hz case, which experiences no buckling in contrast to the single-beam trial. The data sampled in the two-beam case are smoother, with less high-frequency noise; this can be attributed both to a reduction in torsional effects as well as the impact of the altered stiffness on the resonant frequencies of the system.

B. Case Study II: Flapping in Water

This concept has also been demonstrated in water, using a RC servo to produce symmetric flapping while measuring the torques produced by the fluidic interactions. Fig. 8(b) shows frames extracted from a single flapping cycle of a wing with a precurved buckling beam. Frames 1–4 represent the recovery stroke of our sinusoidal control signal; frames 5–8 constitute the power stroke. Hysteresis is clearly visible between these strokes, indicating that the dynamic interactions between inertia, drag, and buckling play a role in deforming the beam anisotropically.

In this experiment, we use a sinusoidal input signal with constant amplitude and variable frequency to study the impact of flapping speed on buckling and torque. Fig. 8(c) shows the torque generated for 0.1, 0.2, 0.3, and 0.4 Hz frequencies over several cycles. The results clearly demonstrate the effect of anisotropic beam buckling. The maximum positive torque increases from 0.05 to 0.43 Nm between 0.1 and 0.4 Hz while the negative torque generated during a flapping cycle is limited across all experiments to no less than –0.12 Nm. Table II shows the comparison between the generated torques in this experiment and values estimated by the dynamic model (Section III). The results of the two-beam design are subsequently shown in Fig. 2. Though illustrative of the tradeoffs between torsional stiffness and buckling, the results show that increased mechanism stiffness increases the torque that can be supported by the beam

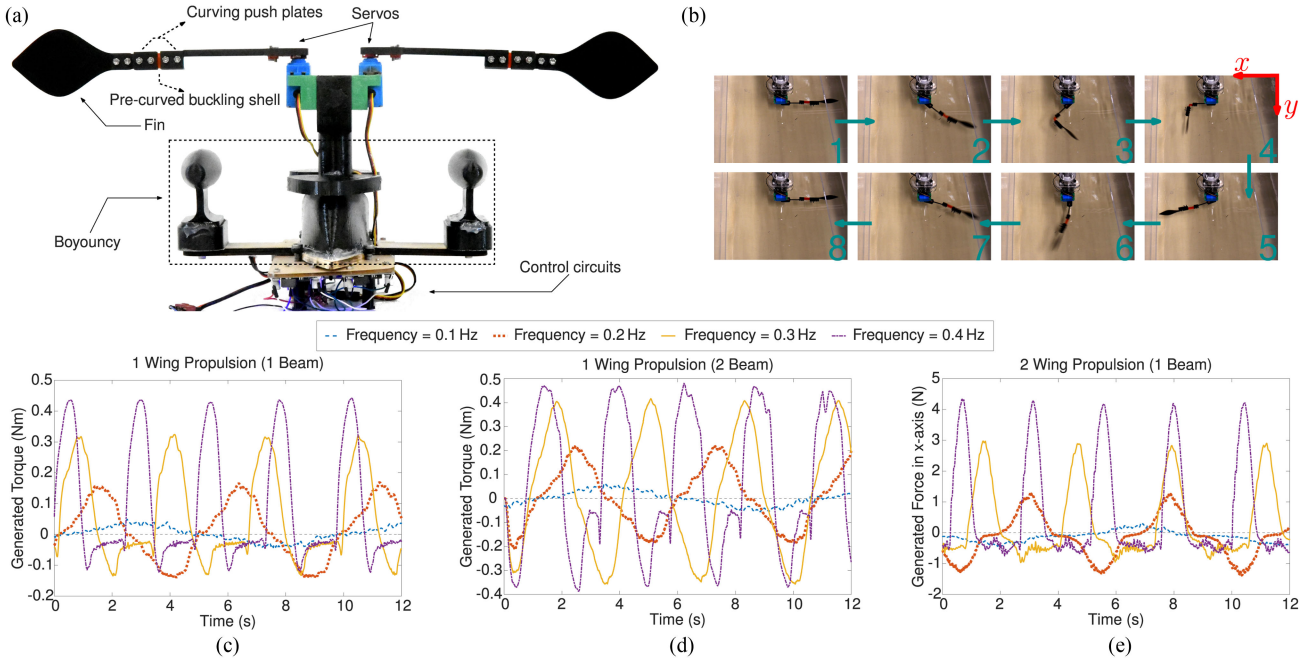

Fig. 8. Effect of asymmetric buckling on a wing flapping in water. (a) This robotic prototype uses buckling to swim through water. (b) Frames extracted from the propulsion test demonstrate buckling in the recovery stroke and no buckling in the power stroke. (c and e) Effect of various flapping rates on the torque produced on a fixed frame for (c) a one-beam wing. (d) Two-beam wing. (e) Thrust produced in the x-axis by two one-beam wings.

TABLE II
GENERATED TORQUES IN SIMULATION AND EXPERIMENTAL

Frequency	Simulation		Experiment		Buckling
	τ_{min} (Nm)	τ_{max} (Nm)	τ_{min} (Nm)	τ_{max} (Nm)	
0.1	-0.04	0.04	-0.04	0.04	No
0.2	-0.14	0.14	-0.14	0.15	No
0.3	-0.23	0.3	-0.13	0.32	One side
0.4	-0.24	0.46	-0.12	0.44	One side

in recovery [Fig. 8(d)], undesirable from the perspective of gait efficiency. This design requires optimization against other design parameters to simultaneously reduce the effect of torsion and increase efficiency.

Using these results, a water-based robotic platform has been developed that leverages buckling during flapping. As illustrated in Fig. 8(a), the robot uses curved beams to connect to two rigid fins made from 0.76 mm fiberglass sheet. The buckling portions of the links are made from a laminated composite of fabric, adhesive and 0.18 mm-thick polyester, which is used to reinforce the material during buckling.

Based on the properties of the curved beam, if the combination of force and moment experienced at the fin is between the equal and opposite-sense buckling values discussed earlier, the curved beam will buckle unidirectionally, resulting in a different angle of attack, which impacts the lift and drag forces acting on the fin by the fluid. As a result, drag on the robot will be different in power stroke and recovery stroke, creating a thrust differential over a gait cycle, which makes the robot swim forward. The magnitude of forces and moments caused by fin propulsion can be adjusted by controlling the amplitude and speed of the servo movements, size of the fin, length of the beam (l), and radius of curvature (r).

The left and right fin servos follow a sinusoidal control signal of the form

$$y_i = A_i \sin(2\pi f_i t + a_i) + b_i \tag{13}$$

where A_i represents an adjustable amplitude, f_i represents the frequency, a_i represents a phase offset, and b_i represents an amplitude offset from the neutral point, which is nominally set to $b_i = 0$ throughout these trials. This symmetric motion about our transverse and bilaterally symmetric robot guarantees that any forward locomotion can be attributed to the changes in drag caused by the buckling curved beam attached to the fin. Fig. 8(e) shows the forward thrust generated by symmetrical flapping of the two wings for 0.1, 0.2, 0.3, and 0.4 Hz frequencies.

In water trials, the swimming robot was able to swim with an average speed of 0.1 m/s when $y_0 = y_1$. The robot was able to rotate by using only one limb at a time. This is important because a nonbuckling fin acts more like a fish caudal fin and causes the robot to move laterally; because of buckling, the fin produces nonzero average torque, resulting in the robot turning. The video attached to the article highlights the motion of the robot.

V. CONCLUSION

This article studies the use of buckling curved beams for use in flapping-wing mobile robots moving through fluids. The theory behind this phenomenon is studied analytically, while

FEA permits us to look beyond the limited conditions anticipated by prior work and investigate a wide range of buckling shapes and load conditions. The proposed propulsion method has been experimentally validated by measuring the force and work generated by a wing flapping in air and water, in the presence and absence of buckling. Hysteresis due to buckling is clearly visible, and the average force produced via symmetric flapping is positive in the direction of forward motion. Finally, a swimming robot based on this phenomenon has been designed and can swim at an approximate average speed of 0.1 m/s using a symmetric flapping strategy. The robot is additionally able to turn when flapping only one fin.

In terms of impact, we believe this work will inform the future design and optimization of simple flapping swimmers and flyers. Understanding the nonlinear behavior of buckling curved beams and how geometry influences critical buckling loads permits these systems to be tuned along a spectrum of performance requirements for use in air or water. Knowledge of how hinge geometry affects such response will also lead to simpler, more mechanism-oriented design approaches, and will permit designers to identify coupled wing/beam designs as well as tuned swimming gaits that are optimal across competing criteria like efficiency, power, and speed.

Future work will explore mechanisms by which buckling limits can be adjusted in real time in response to changing needs. This concept supports new strategies to employ distributed actuation and sensing of curvature as well as multidomain modeling and design strategies that bridge the gap between mechanics, mechanisms, and fluids. Our future goal is to permit the rational design of buckling wings from specification to realization, as well as to demonstrate this concept on high-performance platforms that leverage programmable buckling in order to create biorealistic flapping-wing swimmers and flyers. Future work will expand this concept to include terrestrial locomotion and amphibious environments.

Acknowledgment

The authors would like to thank Y. Jiang, V. P. Gadekar, and A. Doroudchi for their contributions.

References

[1] B. E. Flammang and G. V. Lauder, "Caudal fin shape modulation and control during acceleration, braking and backing maneuvers in bluegill sunfish, lepomis macrochirus," *J. Exp. Biol.*, vol. 212, no. 2, pp. 277–286, 2009.

[2] K. Nguyen, N. Yu, M. M. Bandi, M. Venkadesan, and S. Mandre, "Curvature-induced stiffening of a fish fin," *J. Roy. Soc. Interface*, vol. 14, no. 130, 2017, Art. no. 20170247.

[3] V. Di Santo, E. L. Blevins, and G. V. Lauder, "Batoid locomotion: Effects of speed on pectoral fin deformation in the little skate, leucoraja erinacea," *J. Exp. Biol.*, vol. 220, no. 4, pp. 705–712, 2017.

[4] S. Combes and T. Daniel, "Flexural stiffness in insect wings II. Spatial distribution and dynamic wing bending," *J. Exp. Biol.*, vol. 206, no. 17, pp. 2989–2997, 2003.

[5] J. A. Walker, "Functional morphology and virtual models: Physical constraints on the design of oscillating wings, fins, legs, and feet at intermediate Reynolds numbers," *Integrative Comp. Biol.*, vol. 42, no. 2, pp. 232–242, 2002.

[6] R. J. Wootton, "Geometry and mechanics of insect hindwing fans: A modelling approach," *Proc. Roy. Soc. London. Ser. B, Biol. Sci.*, vol. 262, no. 1364, pp. 181–187, 1995.

[7] S. M. Walker, A. L. Thomas, and G. K. Taylor, "Deformable wing kinematics in the desert locust: How and why do camber, twist and topography vary through the stroke?," *J. Roy. Soc. Interface*, vol. 6, no. 38, pp. 735–747, 2008.

[8] J. Young, S. M. Walker, R. J. Bomphrey, G. K. Taylor, and A. L. Thomas, "Details of insect wing design and deformation enhance aerodynamic function and flight efficiency," *Science*, vol. 325, no. 5947, pp. 1549–1552, 2009.

[9] R. Vogel and H. Stark, "Motor-driven bacterial flagella and buckling instabilities," *Eur. Phys. J. E*, vol. 35, no. 2, 2012, Art. no. 15.

[10] A. Ghatak, A. Majumder, and R. Kumar, "Hysteresis of soft joints embedded with fluid-filled microchannels," *J. Roy. Soc. Interface*, vol. 6, no. 31, pp. 203–208, 2008.

[11] A. G. Volkov, T. Adesina, V. S. Markin, and E. Jovanov, "Kinetics and mechanism of dionaea muscipula trap closing," *Plant Physiol.*, vol. 146, no. 2, pp. 694–702, 2008.

[12] V. S. Markin, A. G. Volkov, and E. Jovanov, "Active movements in plants: Mechanism of trap closure by dionaea muscipula ellis," *Plant Signaling Behav.*, vol. 3, no. 10, pp. 778–783, 2008.

[13] D. Hodick and A. Sievers, "On the mechanism of trap closure of venus flytrap (dionaea muscipula ellis)," *Planta*, vol. 179, no. 1, pp. 32–42, 1989.

[14] K. Saito, S. Nomura, S. Yamamoto, R. Niiyama, and Y. Okabe, "Investigation of hindwing folding in ladybird beetles by artificial elytron transplantation and microcomputed tomography," *Proc. Nat. Acad. Sci.*, vol. 114, no. 22, pp. 5624–5628, 2017.

[15] Y. Wang and M. A. Minor, "Design and evaluation of a soft robotic smart shoe for haptic terrain rendering," *IEEE/ASME Trans. Mechatronics*, vol. 23, no. 6, pp. 2974–2979, Dec. 2018.

[16] D. Drotman, M. Ishida, S. Jadhav, and M. T. Tolley, "Application-driven design of soft, 3-D printed, pneumatic actuators with bellows," *IEEE/ASME Trans. Mechatronics*, vol. 24, no. 1, pp. 78–87, Feb. 2019.

[17] Y. Shin, T. Kim, B. C. Jung, S. Moon, and J. Lee, "Development of hybrid vibration isolator by inertial type actuator and wire mesh mount," *IEEE/ASME Trans. Mechatronics*, vol. 24, no. 3, pp. 1356–1367, Jun. 2019.

[18] K. Seffen, "Mechanical memory metal: A novel material for developing morphing engineering structures," *Scripta Materialia*, vol. 55, no. 4, pp. 411–414, 2006.

[19] A. Pandey, D. E. Moulton, D. Vella, and D. P. Holmes, "Dynamics of snapping beams and jumping poppers," *Europhys. Lett.*, vol. 105, no. 2, 2014, Art. no. 24001.

[20] J.-s. Koh *et al.*, "A modular folded laminate robot capable of multi modal locomotion," in *Proc. Int. Symp. Exp. Robot.*, 2016, pp. 59–70.

[21] S.-W. Kim, J.-S. Koh, J.-G. Lee, J. Ryu, M. Cho, and K.-J. Cho, "Flytrap-inspired robot using structurally integrated actuation based on bistability and a developable surface," *Bioinspiration Biomimetics*, vol. 9, no. 3, 2014, Art. no. 036004.

[22] S.-M. Baek, D.-Y. Lee, and K.-J. Cho, "Curved compliant facet origami-based self-deployable gliding wing module for jump-gliding," in *Proc. ASME Int. Des. Eng. Tech. Conf. Comput. Inf. Eng.*, 2016, Paper DETC2016-60543.

[23] G.-P. Jung, J.-S. Koh, and K.-J. Cho, "Underactuated adaptive gripper using flexural buckling," *IEEE Trans. Robot.*, vol. 29, no. 6, pp. 1396–1407, Dec. 2013.

[24] S. Mintchev, J. Shintake, and D. Floreano, "Bioinspired dual-stiffness origami," *Sci. Robot.*, vol. 3, no. 20, 2018, Art. no. eaau0275.

[25] Y. Jiang, M. Sharifzadeh, and D. Aukes, "Reconfigurable soft flexure hinges via pinched tubes," in *Proc. IEEE/RSJ Int. Conf. Intell. Robot. Syst.* 2020.

[26] N. Kato *et al.*, "Elastic pectoral fin actuators for biomimetic underwater vehicles," in *Proc. Bio-Mechanisms Swimming Flying*, 2008, pp. 271–282.

[27] S. B. Behbahani and X. Tan, "Design and modeling of flexible passive rowing joint for robotic fish pectoral fins," *IEEE Trans. Robot.*, vol. 32, no. 5, pp. 1119–1132, Oct. 2016.

[28] V. A. Pham, T. T. Nguyen, B. R. Lee, and T. Q. Vo, "Dynamic analysis of a robotic fish propelled by flexible folding pectoral fins," *Robotica*, vol. 38, no. 4, pp. 699–718, 2020.

[29] B. Kwak, D. Lee, and J. Bae, "Comprehensive analysis of efficient swimming using articulated legs fringed with flexible appendages inspired by a water beetle," *Bioinspiration Biomimetics*, vol. 14, no. 6, 2019, Art. no. 066003.

[30] A. Simha, R. Gkliva, Ü. Kotta, and M. Kruusmaa, "A flapped paddle-fin for improving underwater propulsive efficiency of oscillatory actuation," *IEEE Robot. Autom. Lett.*, vol. 5, no. 2, pp. 3176–3181, Apr. 2020.

[31] F. A. Naser and M. T. Rashid, "Design, modeling, and experimental validation of a concave-shape pectoral fin of labriform-mode swimming robot," *Eng. Rep.*, vol. 1, 2019, Art. no. e12082.

[32] J. Palmisano, R. Ramamurti, K.-J. Lu, J. Cohen, W. Sandberg, and B. Ratna, "Design of a biomimetic controlled-curvature robotic pectoral fin," in *Proc. IEEE Int. Conf. Robot. Autom.*, 2007, pp. 966–973.
[33] S. J. I. Walker and G. S. Aglietti, "Experimental investigation of tape springs folded in three dimensions," *AIAA J.*, vol. 44, no. 1, pp. 151–159, 2006.
[34] S. P. Timoshenko and J. M. Gere, *Theory of Elastic Stability*, New York, NY, USA: Dover Publications, Mineola, 1961.
[35] E. Kebadze, S. Guest, and S. Pellegrino, "Bistable prestressed shell structures," *Int. J. Solids Struct.*, vol. 41, no. 11–12, pp. 2801–2820, 2004.
[36] Ö. Soykasap, "Analysis of tape spring hinges," *Int. J. Mech. Sci.*, vol. 49, no. 7, pp. 853–860, 2007.
[37] S. Hoffait, O. Brüls, D. Granville, F. Cugnon, and G. Kerschen, "Dynamic analysis of the self-locking phenomenon in tape-spring hinges," *Acta Astronautica*, vol. 66, no. 7–8, pp. 1125–1132, 2010.
[38] W. Wuest, "Some applications of the cylinder shell theory," *J. Appl. Math. Mech./Zeitschrift für Angewandte Mathematik und Mechanik*, vol. 34, no. 12, pp. 444–454, 1954.
[39] K. Seffen, "On the behavior of folded tape-springs," *J. Appl. Mech.*, vol. 68, no. 3, pp. 369–375, 2001.
[40] J. W. Roberts, R. Cory, and R. Tedrake, "On the controllability of fixed-wing perching," in *Proc. IEEE Amer. Control Conf.*, 2009, pp. 2018–2023.
[41] J. P. Whitney, "Design and performance of insect-scale flapping-wing vehicles," Ph.D. dissertation, Dept. School Eng. Appl. Sci., Harvard Univ., Cambridge, MA, USA, 2012.
[42] K. Mazaheri and A. Ebrahimi, "Experimental investigation of the effect of chordwise flexibility on the aerodynamics of flapping wings in hovering flight," *J. Fluids Struct.*, vol. 26, no. 4, pp. 544–558, 2010.
[43] N. Gravish and R. J. Wood, "Anomalous yaw torque generation from passively pitching wings," in *Proc. IEEE Int. Conf. Robot. Autom.*, 2016, pp. 3282–3287.
[44] J. P. Whitney and R. J. Wood, "Aeromechanics of passive rotation in flapping flight," *J. fluid Mech.*, vol. 660, pp. 197–220, 2010.

Mohammad Sharifzadeh received the B.Sc. degree in electrical engineering from Shiraz University, Shiraz, Iran, in 2012 and the M.Sc. degree in mechatronics engineering from the University of Tehran, Tehran, Iran, in 2016. He is currently working toward the Ph.D. degree in systems engineering with Arizona State University, Mesa, AZ, USA.

His research interest include control and identification of foldable robots made by laminating techniques. He is interested in the fields of parallel mechanisms, dynamic and position control of robots, system identification, and analytic control.

Daniel M. Aukes received the B.S. degree in mechanical engineering from Northwestern University, Evanston, IL, USA, in 2004. and the M.S. and Ph.D. degrees in mechanical engineering from Stanford University, Stanford, CA, USA, in 2009 and 2013, respectively.

He is currently an Assistant Professor with the Ira A. Fulton Schools of Engineering, Arizona State University, Mesa, AZ, USA. His Postdoctoral work with Harvard University focused on the design and manufacturing of laminate robots. His current research interests include design and manufacture of affordable mobile robots using dynamics and simulation.